

Illuminating a Contorted Slab with a Complex Intralab Rupture Evolution during the 2021 M_W 7.3 East Cape, New Zealand Earthquake

Ryo Okuwaki^{1,2,3,=}, Stephen P. Hicks^{4,=}, Timothy J. Craig³, Wenyan Fan⁵, Saskia Goes⁴, Tim J. Wright³, and Yuji Yagi²

¹Mountain Science Center, University of Tsukuba, Tsukuba, Ibaraki 305-8572, Japan

²Faculty of Life and Environmental Sciences, University of Tsukuba, Tsukuba, Ibaraki 305-8572, Japan

³COMET, School of Earth and Environment, University of Leeds, Leeds LS2 9JT, UK

⁴Department of Earth Science and Engineering, Imperial College London, London SW7 2AZ, UK

⁵Scripps Institution of Oceanography, UC San Diego, La Jolla, California 92093, USA

Contents of this file

- Texts S1–S4
- Tables S1–S2
- Figures S1–S13

⁼Equally contributing author

Corresponding author: Ryo Okuwaki, rokuwaki@geol.tsukuba.ac.jp

Text S1. Hypocenter relocation

The regional monitoring agency, GeoNet, reported an initial hypocenter depth for the 2021 East Cape earthquake of ~80 km (<https://www.geonet.org.nz/earthquake/history/2021p169083>; last accessed 06/05/2021) before later being revised to an operator-assigned default depth of 12 km. Global monitoring agencies also assigned fixed depths, but waveform-based depths (e.g. centroids) appear to be deeper at ~50 km (Table S2). The global arrival-time based hypocenter estimates with fixed depths also have very large arrival time residuals (>3 s) at the closest stations located within 200 km epicentral distance, suggesting a possible incompatibility with the fixed depth solutions. Given this apparent uncertainty and mismatch in depths, we performed a relocation of the earthquake using stations at local-regional distances. We picked *P*- and *S*-wave arrival times from GeoNet stations (network code: NZ) up to ~1000 km epicentral distance, with each arrival time assigned a weight based on picking uncertainty. The closest station is located at 100 km epicentral distance. We also included arrival times from the station NZ.RAO located to the north on the Kermadec Islands to maximize the azimuthal coverage.

For the relocation, we used the NonLinLoc software (Lomax et al., 2000, 2009), which offers robust constraints on location uncertainties compared with traditional single-event location codes, and in which we employed a travel-time dependent error, effectively giving an epicentral distance weighting. For the velocity model, we took a 1-D profile through the New Zealand Wide 3-D *P*- and *S*-wave velocity model (NZW2.2); (Eberhart-Phillips et al., 2010, 2020). Beneath the area where NZW2.2 has sufficient resolution (~35 km), we merged the velocity model with the global AK135 model (Kennett et al., 1995). Our relocated hypocenter is as follows: time: 2021-03-04T13:27:35.71; latitude: -37.466°; longitude: 179.774°; depth 72 km, with an overall RMS residual of 0.63 s, which is acceptable given the large station distances considered. Residuals at the closest stations are small - for example at station MXZ, located at 120 km epicentral distance, the *P*-wave residual is 0.3 s, whereas for the USGS-NEIC solution, it is 3.3 s. The 68% confidence ellipsoid of our solution corresponds to an epicentral uncertainty of 0.03 and 0.02 degrees in longitude and latitude, respectively; the depth uncertainty is ± 9 km (see Fig. S1). We also found that this hypocenter location was robust if we instead used the AK135 global velocity model (Kennett et al., 1995).

Text S2. *W*-phase CMT inversion

To gain a first-order approximation of the earthquake source, we performed a moment tensor inversion using long-period regional and teleseismic waveforms (Fig. S3). We used the Grond software (Heimann et al., 2018) which uses a Bayesian bootstrapping in a probabilistic optimisation method to fully explore the solution space, and resulting uncertainties and parameter trade-offs. We used stations from the G, GT, II, and IU seismic networks located within epicentral distances of 5–90 degrees. We defined the *W*-phase window and frequency bandpass of 2.0–8.5 mHz based on Duputel et al. (2012). Our window includes a long-period taper on either side of the predicted *W*-phase window, which includes surface waves that help to better constrain source depth (e.g., Ye et al., 2017). The best-fitting source duration of 30–35 s is consistent with the source time function from the teleseismic finite fault model (Fig. 3). The full report of the inversion result, including the waveform fits and the model uncertainties is available at <https://rokuwaki.github.io/2021EastCapeNZ/grond-report/>.

Text S3. Regional centroid moment tensor (R-CMT) inversion

For R-CMT inversion, we computed Green's functions in a 1-D seismic velocity profile from the NZW2.1 velocity model described in the section above. We used the ISOLA software (Sokos & Zahradnik, 2008), which inverts for waveforms in the time domain to compute moment tensors. ISOLA searches across a prescribed grid of trial-point sources to find the deviatoric centroid moment tensor (CMT) in space and time that maximizes the fit between the observed and synthetic waveforms. We used available strong motion and broadband waveforms from the GeoNet network (network code: NZ; Petersen et al., 2011) located up to ~400 km epicentral distance and removed the instrument responses. We carefully chose waveforms unaffected by clipping and non-linear tilting due to strong ground motion from the earthquake. We found that weighting the waveforms equally by epicentral distance produced the most stable results.

Low frequency, single source inversion, grid search over depth

We first inverted for a single-point source moment tensor solution using long-period waveforms (50–100s period), searching over a grid of trial point sources between 3 km and 139 km depth with a grid spacing of 4 km, located beneath our re-located epicenter. The best-fitting solution gives a centroid depth of 71 km with a faulting mechanism of oblique-reverse faulting, striking roughly east-west (see Fig. S4). This mechanism is consistent with the focal mechanisms of the earthquake reported by global monitoring agencies (USGS-NEIC, GFZ-GEOFON, IPGP-GEOSCOPE; Fig. S10). Correlation as function of depth (Fig. S4) also shows a weaker local maxima in waveform correlation with a normal faulting mechanism at <12 km depth, a consistent feature that we discuss further below.

Higher frequency, multiple source inversion, grid search over depth

To investigate source complexity, we increased the upper frequency corner in the inversion to 0.04 Hz (25 s) and resolved multiple sub-events using a 25 s long triangular moment-rate function (Fig. S5). The first sub-event (M_W 7.3) has the oblique-thrusting mechanism found above, with a centroid time of +11 s from the origin time (OT) and depth of 71 km. The second sub-event (M_W 6.8) has a mechanism of trench-parallel normal faulting, and has a centroid time of OT+17 s and a depth of 7 km. Addition of the second sub-event significantly increases the total waveform variance reduction (VR) by 24%. This normal faulting sub-event is more consistent with the solution reported by GeoNet (Fig. S10). This configuration of deep sub-event followed by shallow sub-event is consistent with the overall local correlation minima seen in the low-frequency solution (Text S3).

Higher frequency, multiple source inversion, grid search a 2-D trench-parallel oriented plane

In a final step, we solved for multiple sub-events on a trench-parallel plane of trial point sources, similar to the teleseismic slip-rate inversion above (although with a coarser grid spacing of 10 km along-strike and down-dip (Fig. S6). We also tested a trench-normal plane; however this configuration produced an overall poorer fit to waveforms. The resulting solution is similar to those above, aside from Sub-event 1 shifts 20–30 km north of the epicenter, and has a slightly shallower depth of 52 km.

Text S4. Finite-fault potency-density inversion

We use the flexible finite-fault inversion method developed by Shimizu et al. (2020). The method considers the uncertainty of the Green's function by adopting the formulation of Yagi and Fukahata (2011), which explicitly introduces the error term of the Green's function into the data covariance matrix. The method also considers the uncertainty of fault geometry by representing the fault deformation by the superposition of five-basis double couple components (Kikuchi & Kanamori, 1991), which solves a spatiotemporal distribution of potency density (Ampuero & Dahlen, 2005). The finite-fault potency inversion (Shimizu et al., 2020) adopted in this study has been proven efficient to flexibly model complex rupture evolution of large earthquakes (Okuwaki et al., 2020; Tadapansawut et al., 2021; Yamashita et al., 2021), which is suited for estimating the unknown fault geometry and the non-smooth rupture evolution related to the geometric complexity of the fault system.

We use the vertical component of the teleseismic P waveforms at 55 stations (Fig. S11). The first motion of the P wave is manually picked. The data are selected to ensure azimuthal coverage and with the high signal-to-noise ratio (e.g., Okuwaki et al., 2016). The data are then deconvolved into velocity at 0.6 s sampling interval. The Green's functions are calculated based on the method of Kikuchi and Kanamori (1991). We used the ak135 model (Kennett et al., 1995) to calculate travel time, ray parameter, and geometric spreading factors. The CRUST1.0 model (Laske et al., 2013) is used for the one-dimensional layered medium near the source region to calculate Haskell propagator in Green's functions (Table S1). We do not apply a low-pass filter to both the observed waveforms and Green's functions, which is intended to retrieve the detailed rupture process recorded in higher frequency components (e.g., Shimizu et al., 2020).

We use a model-plane geometry for the finite-fault model, based on the 1-week aftershock distribution (GeoNet, 2021), adopting 200° strike and 90° dip angles. The rectangular finite-fault dimension is 70-km length and 120-km width, and the grid-ding intervals of sub-faults are 5 km \times 10 km along the strike and dip directions. The slip-rate function for each source element on the model fault is represented by the linear B-splines at the temporal interval of 0.6 s. The total source duration is set as 33 s. The maximum rupture velocity is set at 5 km/s, which is fast enough to track a possible fast-propagating rupture front limited by the local shear-wave velocity near the source region (Table. S1). We use the relocated hypocenter 37.466°S , 179.774°E , and 72-km depth for the initial rupture point.

In order to evaluate a modeling sensitivity to selection of a priori model parameters, we test different model-fault geometries and the nucleation depths (Fig. S12). To evaluate a model geometry, we test the horizontal model planes with 0° -dip angle placed at different depths and a vertical model plane with 110° -strike and 90° -dip angles. To evaluate a preferred nucleation depth, we hypothesize the different nucleation depths from 7 to 107 km depths at an interval of 10 km on the optimal model geometry with the 200° -strike and 90° -dip angles. We find that the model favors a deep rupture nucleation, and the slip also favors a deeper part in slab, which lowers the variance between the observed waveforms and the synthetic waveforms calculated as (Shimizu et al., 2021):

$$\text{Variance} = \frac{\sum_j \sum_t (u_j^{\text{obs}}(t) - u_j^{\text{syn}}(t))^2}{\sum_j \sum_t (u_j^{\text{obs}}(t))^2}, \quad (1)$$

where $u_j^{\text{obs}}(t)$ and $u_j^{\text{syn}}(t)$ are the observed and synthetic waveforms at j th station. We also find that the north-south striking fault (strike/dip = $200^\circ/90^\circ$, *Variance*: 0.26) better explains the observed waveforms than the east-west striking fault (strike/dip = $110^\circ/90^\circ$, *Variance*: 0.28). Based on these sensitivity tests, we adopt a model-plane geometry of the 200° -strike and 90° -dip angles with the rupture nucleation point at the relocated hypo-depth of 72 km as our optimal model-plane geometry, which the entire discussions presented in this study are based on.

Resolvability of the complex source process of the 2021 East Cape earthquake has been verified by a synthetic recovery test of the real solution (Fig. S13). We use our optimal source model as an input model, and perform the same inversion procedure written above. The input model is well reproduced, including the complex fault geometry.

Table S1. Near-source structure used for calculating Green’s functions for the finite-fault inversion.

V_P (km/s)	V_S (km/s)	Density (g/cm ³)	Thickness (km)
1.50	0.00	1.02	2.64
6.00	3.50	2.72	1.52
6.60	3.80	2.86	2.28
7.10	3.90	3.05	3.79
8.29	4.59	3.41	- (below moho)

Table S2. Reported earthquake depths from monitoring agencies.

	Agency	Depth (km)
Arrival time based hypocentres	USGS-NEIC ¹	10*
	GFZ-GEOFON ²	35*
	GeoNet ³	12*
	Local-regional relocation (this study)	72
Waveform based solutions	USGS-NEIC <i>W</i> -phase centroid ⁴	51
	IPGP-GEOSCOPE ⁵	45
	Global-CMT ⁶	52
	Regional CMT (this study; 50–100 s period)	71

*fixed depth

¹ U.S. Geological Survey Earthquake Hazards Program (2017)

² Bormann (2012)

³ GeoNet (2021)

⁴ U.S. Geological Survey Earthquake Hazards Program (2017); Duputel et al. (2012)

⁵ Vallée et al. (2011); Vallée (2013)

⁶ Dziewonski et al. (1981); Ekström et al. (2012)

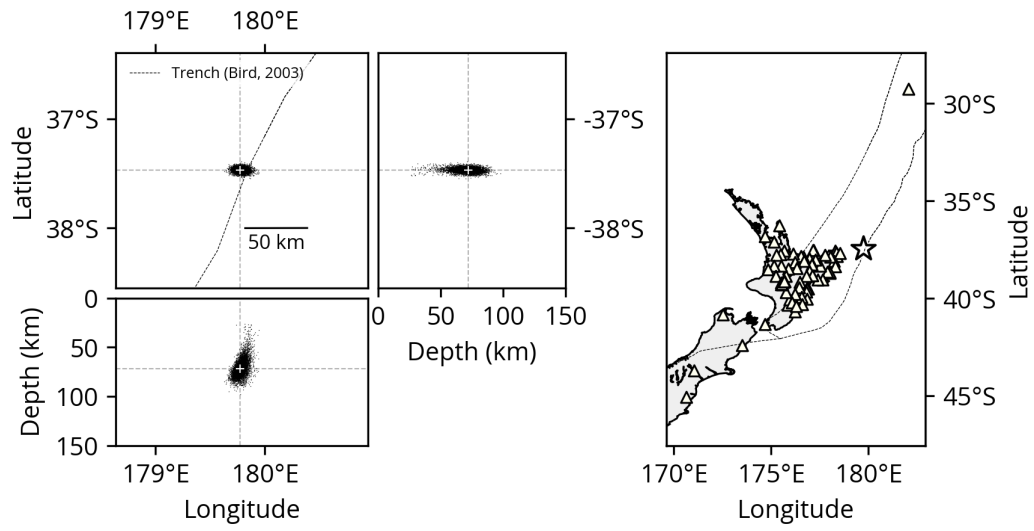


Figure S1. Relocation result. Left panels show the map and cross-sections of the sample locations. The cross marker shows the relocated hypocenter. The small black dots indicate the scatter cloud samples from the hypocentre probability density function. Right panel shows the station distribution (triangle) and the relocated epicenter (star). The dashed lines are the plate boundaries (Bird, 2003).

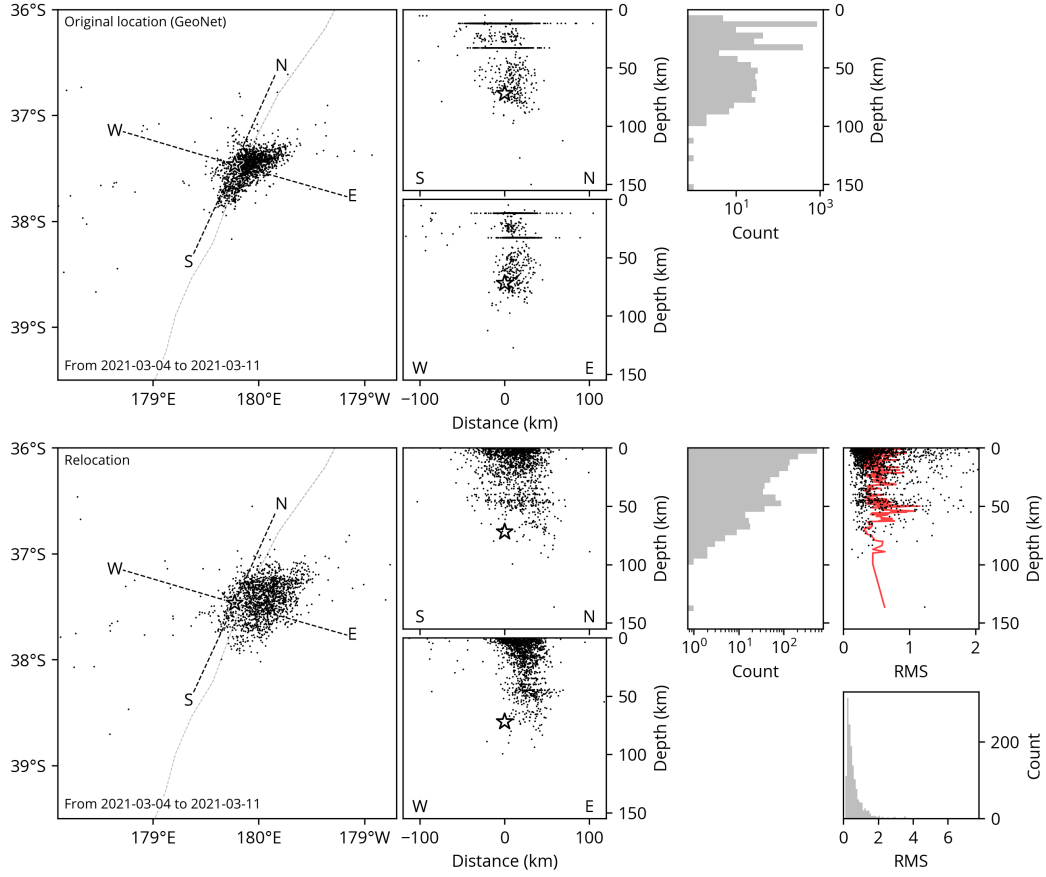


Figure S2. 1-week aftershock distribution. The top panels show the original location by GeoNet (2021). The histogram shows the event counts every 5-km bin. The dashed line is the trench (Bird, 2003). The bottom panels show our relocated result using COMPILE (Lin & Shearer, 2005, 2006). The dot shows the root-mean-square (RMS) value for each relocation, representing the time difference between the phase-pick arrivals and the predicted arrivals from the relocated event for the adopted velocity model. The red line shows the median of the RMS values in a moving window of every 10 counts of the events from shallow to deep. The distribution of the RMS values is shown in a bottom panel.

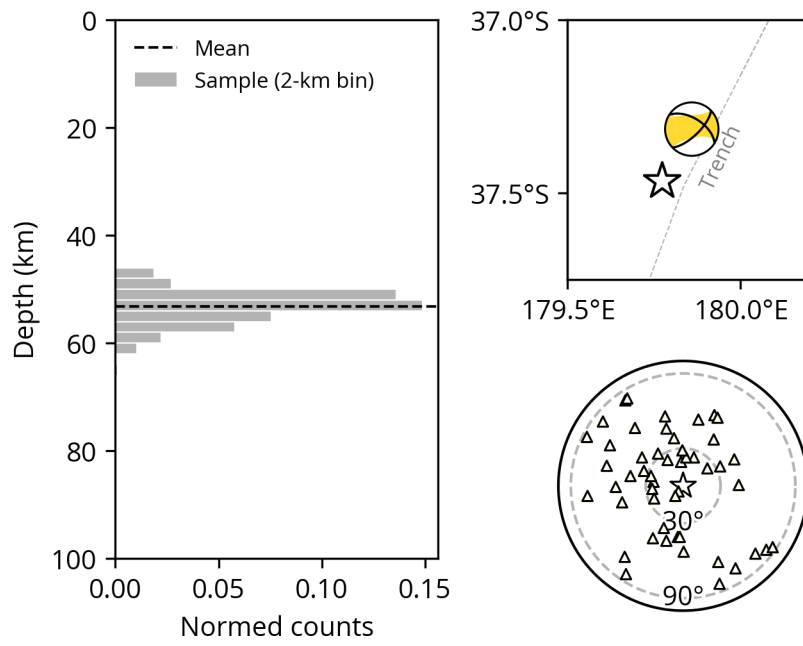


Figure S3. Result of our *W*-phase moment tensor inversion. Left panel shows the histogram of the sample distribution in centroid depth. Right-top panel shows the centroid location (beachball) and the relocated epicenter (star). The dashed line is the trench (Bird, 2003). Right-bottom panel is an azimuthal equidistant projection of the station distribution (triangle). The star shows the centroid location. The dashed lines are the epicentral distances at 30° and 90°.

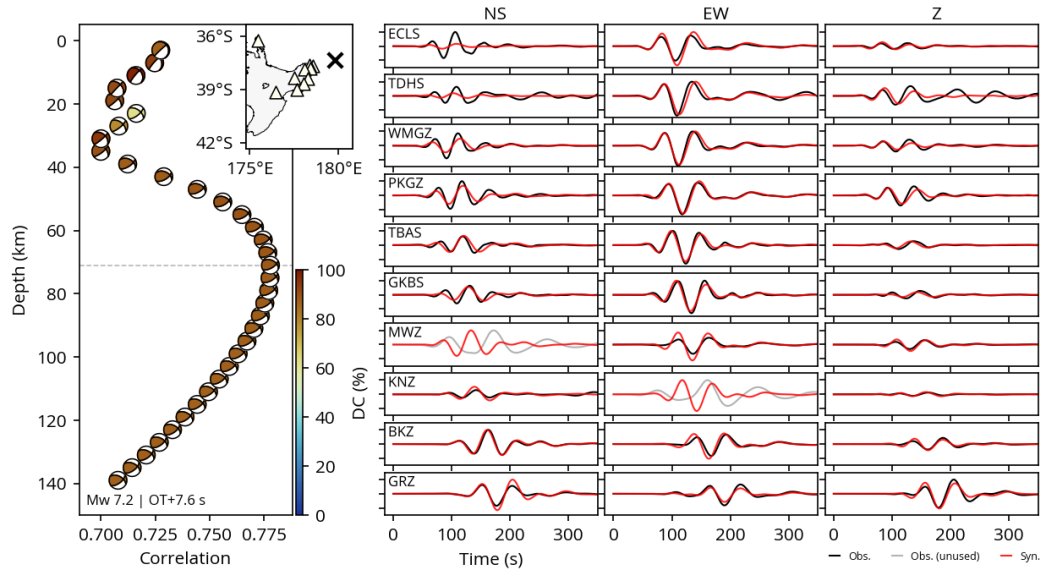


Figure S4. Results from low-frequency, single source regional centroid moment tensor inversion. The left-hand panel shows waveform correlation as a function of depth, and the corresponding double couple solution from best-fitting CMT at each depth. The horizontal gray dashed line shows the best-fitting centroid depth. The inset map shows the stations used in the inversion. The right-hand panel shows the waveform fits (50–100 s period) for the north-south (NS), east-west (EW), and vertical (Z) components. The station code is denoted on each panel.

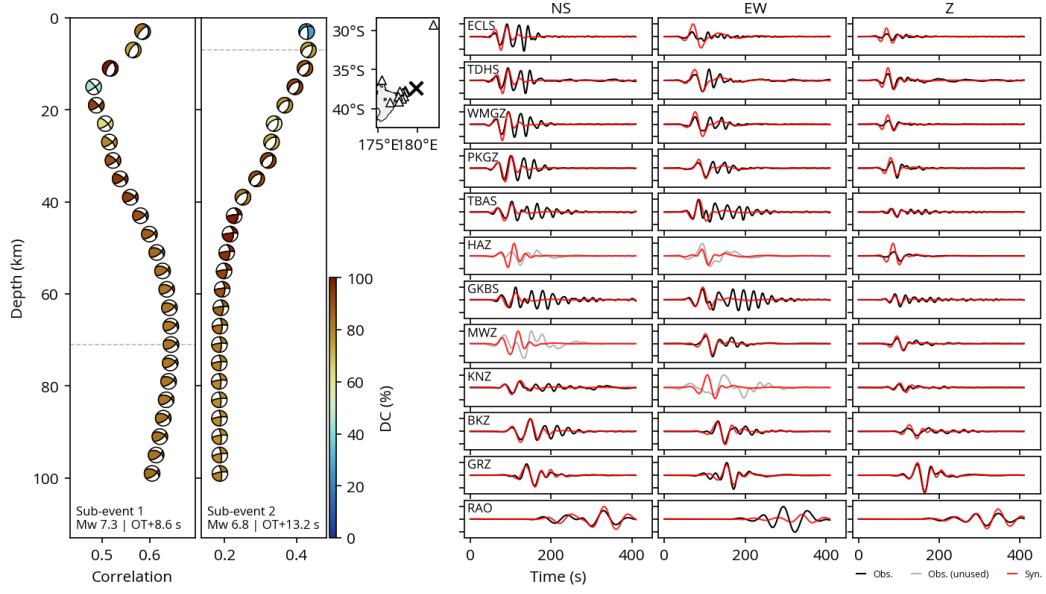


Figure S5. Results from high-frequency, two-point-source regional centroid moment tensor inversion, searching over a line of depth trial point sources. The left-hand panel shows waveform correlation as a function of depth for both sub-events, and the corresponding double couple solution from best-fitting CMTs at each depth. The horizontal gray dashed line shows the best-fitting centroid depth in each case. The inset map shows the stations used in the inversion. The right-hand panel shows the waveform fits (25–100 s period) for the north-south (NS), east-west (EW), and vertical (Z) components. The station code is denoted on each panel.

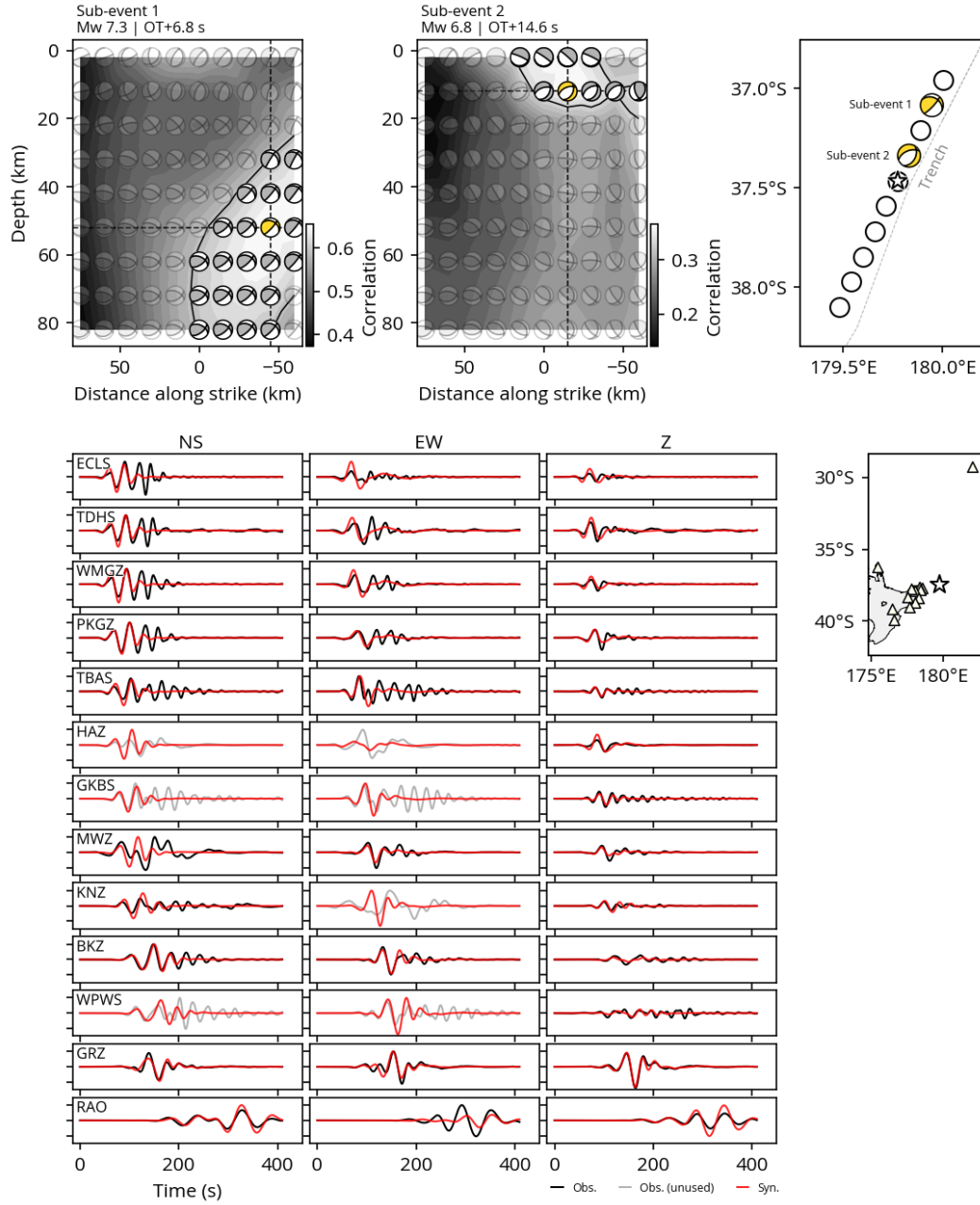


Figure S6. Results from high-frequency, two-point-source regional centroid moment tensor inversion, searching over 2-D trench-parallel oriented plane. The top panels show waveform correlation in a 2D search area for sub-events 1 and 2. The horizontal locations of the searching grid are shown in the right-top panel with the star showing the relocated epicenter and the dashed line as a trench (Bird, 2003). The background colour shows the waveform correlation between the observed and synthetic waveforms. The contour shows the 90% of maximum correlation. The yellow beachball is the corresponding double couple solution from best-fitting CMT. The gray dashed lines show the best-fitting centroid location in each case. The right-bottom map shows the stations (triangle) used in the inversion and the relocated epicenter (star). The left-bottom panel shows the waveform fits (25–100 s period) for the north-south (NS), east-west (EW), and vertical (Z) components. The station code is denoted on each panel.

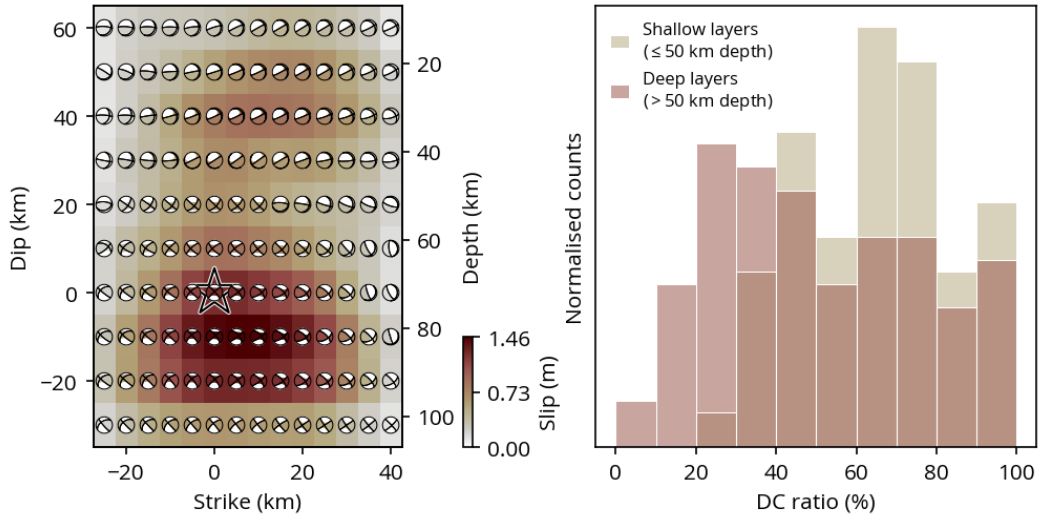


Figure S7. Double-couple percentage (%) for each source element of the finite-fault model. The left panel shows the cross section of the optimal finite-fault model. The beach ball shows a lower-hemisphere stereographic projection of the moment-tensor solution, which is not rotated according to the model geometry, but from top view. The right panel shows the histograms of double-couple (DC) ratio of the moment tensor solutions for the shallow and deep layers.

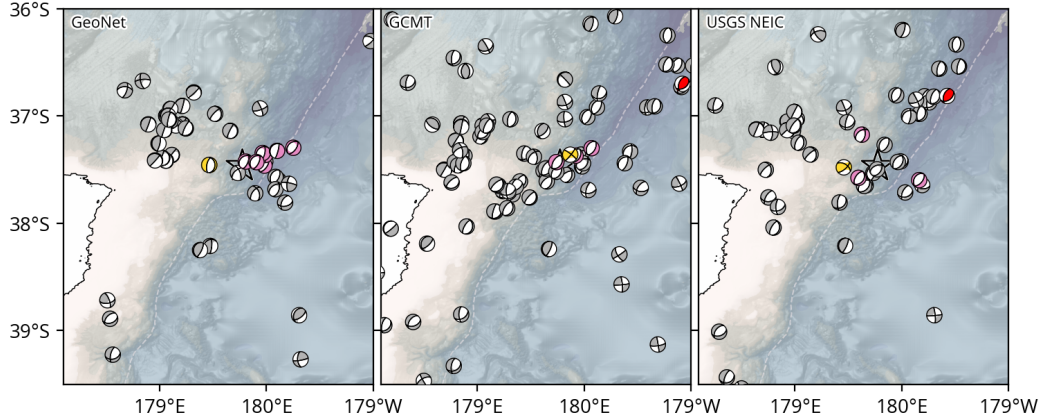


Figure S8. Centroid moment tensor solutions in the study area for the events M_W 5 or larger before 11th March 2021 from GeoNet (2021), the GCMT project (Dziewonski et al., 1981; Ekström et al., 2012), and the USGS NEIC (U.S. Geological Survey Earthquake Hazards Program, 2017). The yellow beachball is the 2021 East Cape earthquake. Grey and pink beach balls indicate events from before and after the 2021 East Cape earthquake, respectively. Red beachball is the solution for the M_W 7.1 2001-08-21 earthquake (not registered in GeoNet (2021) catalog). The dashed line gives the approximate location of the subduction trench (e.g., Bassett et al., 2010). The star marks our relocated epicenter.

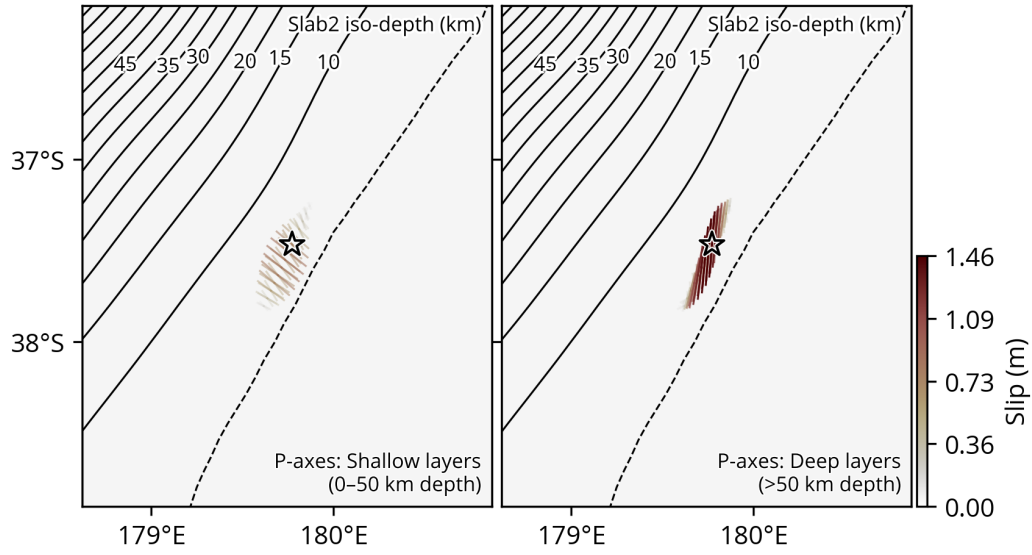


Figure S9. The comparison between the P-axis azimuth distribution from our finite fault model (Fig. 2) and the Slab2 model (Hayes, 2018; Hayes et al., 2018).

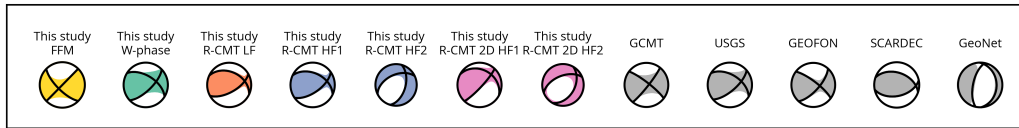


Figure S10. Compilation of CMT solutions for the 2021 East Cape earthquake. Colored beach balls are the various results of this study; gray beach balls are those reported by external agencies. FFM: Finite-fault model (total moment tensor calculated by integration of spatio-temporal moment-density tensors). W-phase: W-phase moment tensor inversion using regional and teleseismic data. R-CMT LF; Single source, low-frequency regional CMT solution. R-CMT HF1 and HF2; Higher frequency, multiple source R-CMT inversion, grid search over depth. R-CMT 2D HF1 and 2D HF2; Higher frequency, multiple source R-CMT inversion, grid search a 2-D trench-parallel oriented plane. GCMT solution (Dziewonski et al., 1981; Ekström et al., 2012). USGS W-phase moment tensor solution (U.S. Geological Survey Earthquake Hazards Program, 2017; Duputel et al., 2012). GEOFON standard inversion using body and surface waves (Bormann, 2012). SCARDEC focal mechanism (Vallée et al., 2011; Vallée, 2013). GeoNet moment tensor (GeoNet Moment Tensors, 2021).

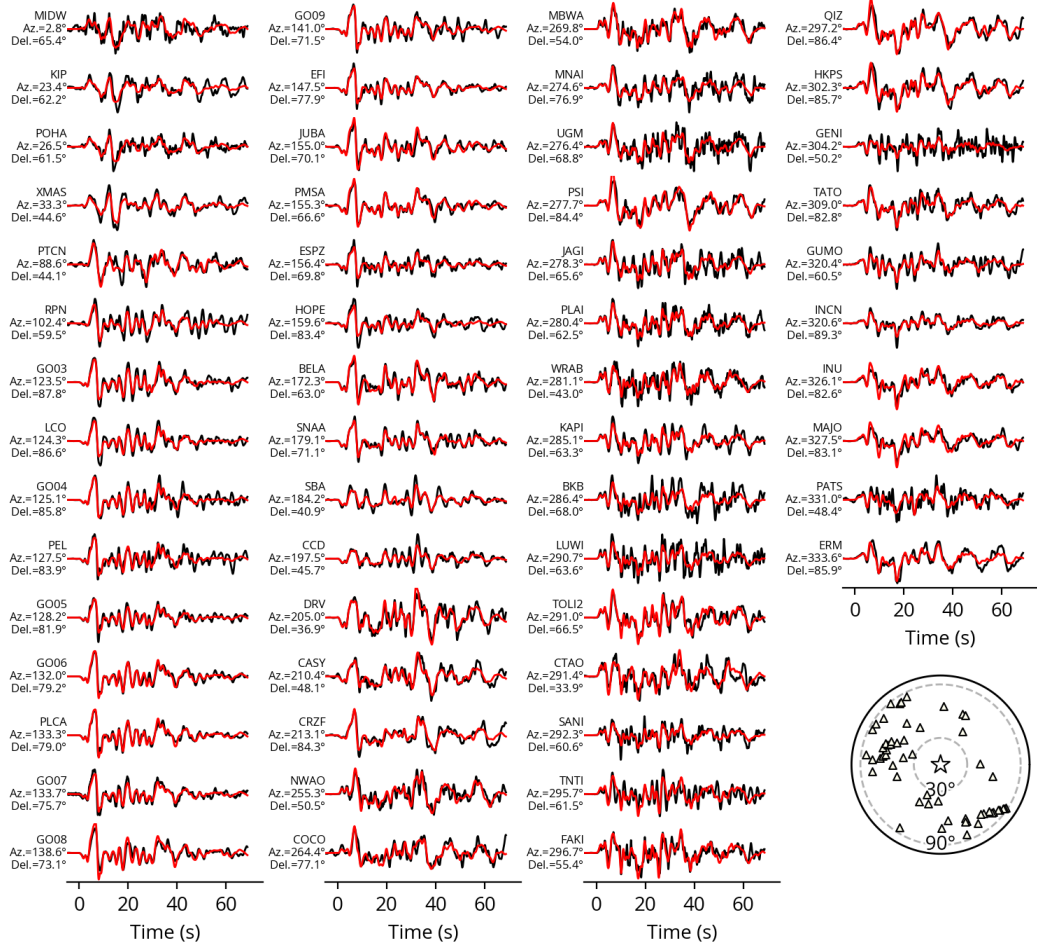


Figure S11. Waveform fitting between the observed (black) and the synthetic waveforms (red) for the optimal finite-fault model with the station code, azimuth, and epicentral distance from the epicenter. The inset is the azimuthal equidistant projection of the station distribution (triangle). The star shows the epicenter, and the dashed lines are the epicentral distances at 30° and 90°.

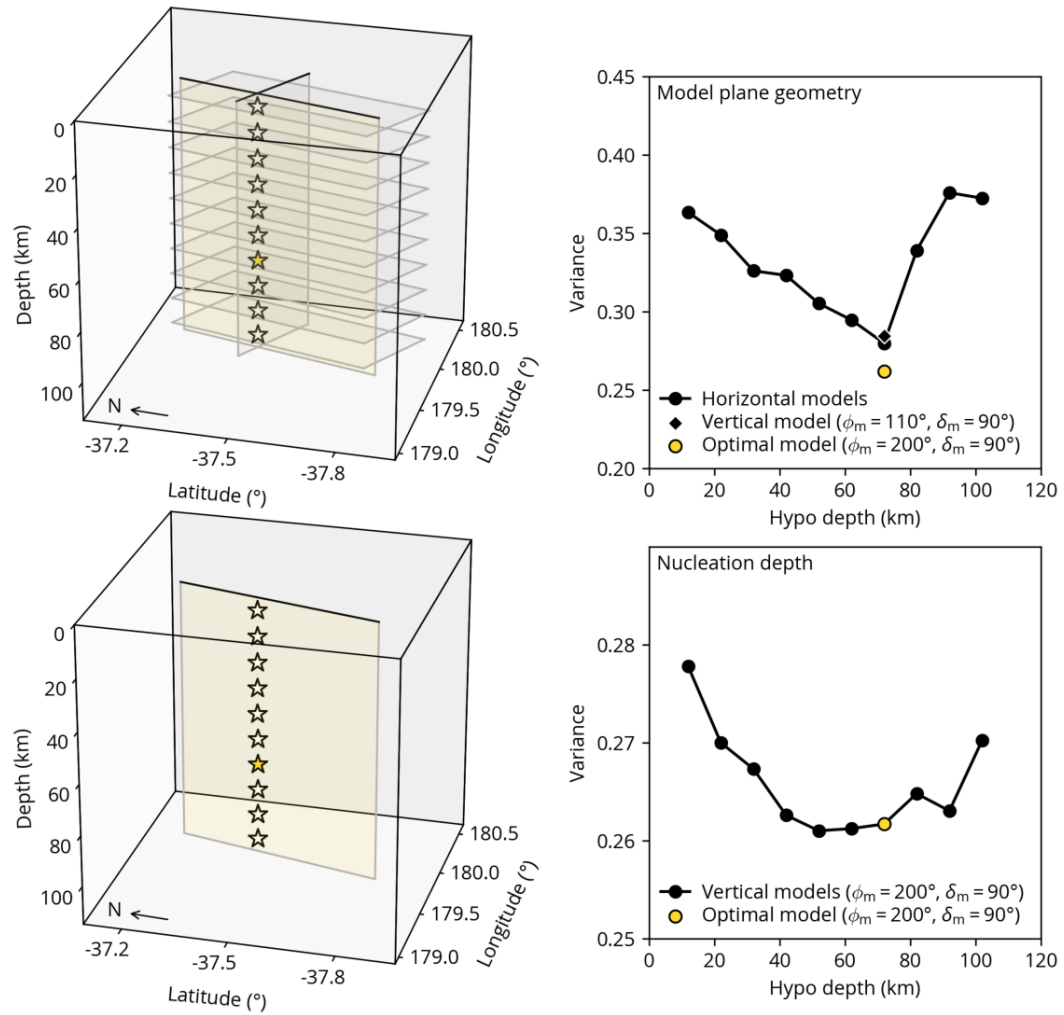


Figure S12. Summary of sensitivity tests for the finite-fault modeling. The left panels show the model-plane geometries and the initial rupture point (star). The yellow panel and the yellow star correspond to the optimal model in each case. The right panels show the variance (waveform fits) distributions. ϕ_m and δ_m represent the : model strike and model dip angles.

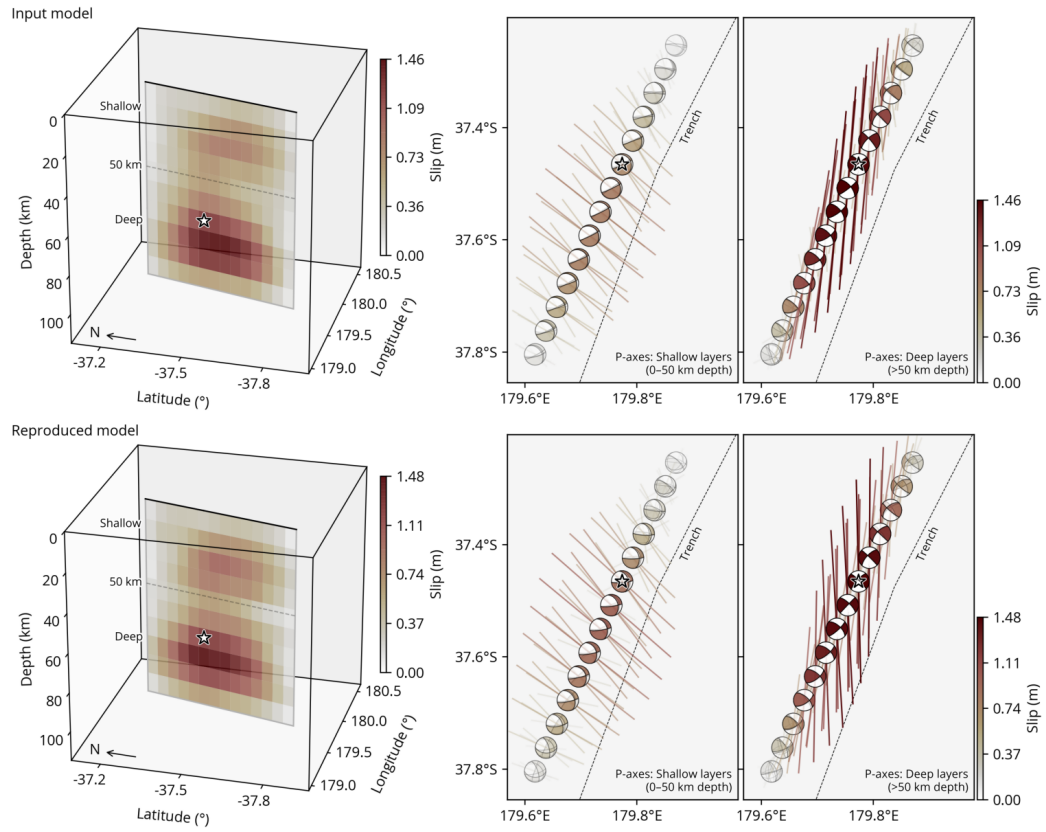


Figure S13. Synthetic test for the finite-fault inversion. The top panels show the input model from the optimal finite-fault model (Fig. 2). The bottom panels show the inverted solution using the synthetic waveforms forward-calculated from the input model. The inversion procedure is the same as used for obtaining the optimal model, described in Text S4.

References

- Ampuero, J.-P., & Dahlen, F. A. (2005). Ambiguity of the Moment Tensor. *Bull. Seismol. Soc. Am.*, 95(2), 390–400. doi:10.1785/0120040103
- Bassett, D., Sutherland, R., Henrys, S., Stern, T., Scherwath, M., Benson, A., ... Henderson, M. (2010). Three-dimensional velocity structure of the northern Hikurangi margin, Raukumara, New Zealand: Implications for the growth of continental crust by subduction erosion and tectonic underplating. *Geochemistry, Geophys. Geosystems*, 11(10). doi:10.1029/2010GC003137
- Bird, P. (2003). An updated digital model of plate boundaries. *Geochemistry, Geophys. Geosystems*, 4(3), 1105. doi:10.1029/2001GC000252
- Bormann, P. (2012). New Manual of Seismological Observatory Practice (NMSOP-2). *IASPEI, GFZ Ger. Res. Cent. Geosci.* doi:10.2312/GFZ.NMSOP-2
- Duputel, Z., Rivera, L., Kanamori, H., & Hayes, G. (2012). W phase source inversion for moderate to large earthquakes (1990-2010). *Geophys. J. Int.*, 189(2), 1125–1147. doi:10.1111/j.1365-246X.2012.05419.x
- Dziewonski, A. M., Chou, T.-A., & Woodhouse, J. H. (1981). Determination of earthquake source parameters from waveform data for studies of global and regional seismicity. *J. Geophys. Res. Solid Earth*, 86(B4), 2825–2852. doi:10.1029/JB086iB04p02825
- Eberhart-Phillips, D., Bannister, S., Reyners, M., & Henrys, S. (2020). *New Zealand Wide model 2.2 seismic velocity and Qs and Qp models for New Zealand*. Zenodo. doi:10.5281/zenodo.3779523
- Eberhart-Phillips, D., Reyners, M., Bannister, S., Chadwick, M., & Ellis, S. (2010). Establishing a versatile 3-D seismic velocity model for New Zealand. *Seismol. Res. Lett.*, 81(6), 992–1000. doi:10.1785/gssrl.81.6.992
- Ekström, G., Nettles, M., & Dziewoński, A. (2012). The global CMT project 2004–2010: Centroid-moment tensors for 13,017 earthquakes. *Phys. Earth Planet. Inter.*, 200–201, 1–9. doi:10.1016/j.pepi.2012.04.002
- GeoNet. (2021). *GeoNet Earthquake Catalog*. Retrieved from https://www.geonet.org.nz/data/types/eq_catalogue
- GeoNet Moment Tensors. (2021). *GeoNet Moment Tensors*. Retrieved from <https://github.com/GeoNet/data/tree/main/moment-tensor>
- Hayes, G. P. (2018). *Slab2 - A Comprehensive Subduction Zone Geometry Model: U.S. Geological Survey data release*. doi:10.5066/F7PV6JNV
- Hayes, G. P., Moore, G. L., Portner, D. E., Hearne, M., Flamme, H., Furtney, M., & Smoczyk, G. M. (2018). Slab2, a comprehensive subduction zone geometry model. *Science*, 362(6410), 58–61. doi:10.1126/science.aat4723
- Heimann, S., Isken, M., Kühn, D., Sudhaus, H., Steinberg, A., Vasyura-Bathke, H., ... Dahm, T. (2018). *Grond - A probabilistic earthquake source inversion framework*. Retrieved from <http://pyrocko.org/grond/docs/current/> doi:10.5880/GFZ.2.1.2018.003
- Kennett, B. L., Engdahl, E. R., & Buland, R. (1995). Constraints on seismic velocities in the Earth from traveltimes. *Geophys. J. Int.*, 122(1), 108–124. doi:10.1111/j.1365-246X.1995.tb03540.x
- Kikuchi, M., & Kanamori, H. (1991). Inversion of complex body waves-III. *Bull. Seism. Soc. Am.*, 81(6), 2335–2350. Retrieved from <https://pubs.geoscienceworld.org/ssa/bssa/article-abstract/81/6/2335/102472/> Inversion-of-complex-body-waves-III
- Laske, G., Masters, T. G., Ma, Z., & Pasyanos, M. (2013). Update on CRUST1.0 - A 1-degree Global Model of Earth's Crust. *Geophys. Res. Abstr.* 15, Ab-

- str. EGU2013-2658, 15, Abstract EGU2013-2658. Retrieved from <https://igppweb.ucsd.edu/~gabi/crust1.html>
- Lin, G., & Shearer, P. (2005). Tests of relative earthquake location techniques using synthetic data. *J. Geophys. Res. Solid Earth*, 110(B4), 1–14. doi:10.1029/2004JB003380
- Lin, G., & Shearer, P. (2006). The COMLOC Earthquake Location Package. *Seismol. Res. Lett.*, 77(4), 440–444. doi:10.1785/gssrl.77.4.440
- Lomax, A., Michelini, A., & Curtis, A. (2009). Earthquake Location, Direct, Global-Search Methods BT - Encyclopedia of Complexity and Systems Science. *Encycl. Complex. Syst. Sci.*, 2449–2473. doi:10.1007/978-0-387-30440-3_150
- Lomax, A., Virieux, J., Volant, P., & Berge-Thierry, C. (2000). Probabilistic Earthquake Location in 3D and Layered Models BT - Advances in Seismic Event Location. In C. H. Thurber & N. Rabinowitz (Eds.), (pp. 101–134). Dordrecht: Springer Netherlands. doi:10.1007/978-94-015-9536-0_5
- Okuwaki, R., Hirano, S., Yagi, Y., & Shimizu, K. (2020). Inchworm-like source evolution through a geometrically complex fault fueled persistent supershear rupture during the 2018 Palu Indonesia earthquake. *Earth Planet. Sci. Lett.*, 547, 116449. doi:10.1016/j.epsl.2020.116449
- Okuwaki, R., Yagi, Y., Aránguiz, R., González, J., & González, G. (2016). Rupture Process During the 2015 Illapel, Chile Earthquake: Zigzag-Along-Dip Rupture Episodes. *Pure Appl. Geophys.*, 173(4), 1011–1020. doi:10.1007/s00024-016-1271-6
- Petersen, T., Gledhill, K., Chadwick, M., Gale, N. H., & Ristau, J. (2011). The New Zealand National Seismograph Network. *Seismol. Res. Lett.*, 82(1), 9–20. doi:10.1785/gssrl.82.1.9
- Shimizu, K., Yagi, Y., Okuwaki, R., & Fukahata, Y. (2020). Development of an inversion method to extract information on fault geometry from teleseismic data. *Geophys. J. Int.*, 220(2), 1055–1065. doi:10.1093/gji/ggz496
- Shimizu, K., Yagi, Y., Okuwaki, R., & Fukahata, Y. (2021). Construction of fault geometry by finite-fault inversion of teleseismic data. *Geophys. J. Int.*, 224(2), 1003–1014. doi:10.1093/gji/ggaa501
- Sokos, E. N., & Zahradnik, J. (2008). ISOLA a Fortran code and a Matlab GUI to perform multiple-point source inversion of seismic data. *Comput. Geosci.*, 34(8), 967–977. doi:10.1016/j.cageo.2007.07.005
- Tadapansawut, T., Okuwaki, R., Yagi, Y., & Yamashita, S. (2021). Rupture Process of the 2020 Caribbean Earthquake Along the Oriente Transform Fault, Involving Supershear Rupture and Geometric Complexity of Fault. *Geophys. Res. Lett.*, 48(1), 1–9. doi:10.1029/2020GL090899
- U.S. Geological Survey Earthquake Hazards Program. (2017). *Advanced National Seismic System (ANSS) Comprehensive Catalog of Earthquake Events and Products*. doi:10.5066/F7MS3QZH
- Vallée, M. (2013). Source time function properties indicate a strain drop independent of earthquake depth and magnitude. *Nat. Commun.*, 4, 1–6. doi:10.1038/ncomms3606
- Vallée, M., Charléty, J., Ferreira, A. M., Delouis, B., & Vergoz, J. (2011). SCARDEC: A new technique for the rapid determination of seismic moment magnitude, focal mechanism and source time functions for large earthquakes using body-wave deconvolution. *Geophys. J. Int.*, 184(1), 338–358. doi:10.1111/j.1365-246X.2010.04836.x
- Yagi, Y., & Fukahata, Y. (2011). Introduction of uncertainty of Green’s function into

- waveform inversion for seismic source processes. *Geophys. J. Int.*, 186(2), 711–720. doi:10.1111/j.1365-246X.2011.05043.x
- Yamashita, S., Yagi, Y., Okuwaki, R., Shimizu, K., Agata, R., & Fukahata, Y. (2021). Consecutive ruptures on a complex conjugate fault system during the 2018 Gulf of Alaska earthquake. *Sci. Rep.*, 11(1), 5979. doi:10.1038/s41598-021-85522-w
- Ye, L., Lay, T., Bai, Y., Cheung, K. F., & Kanamori, H. (2017). The 2017 Mw 8.2 Chiapas, Mexico, Earthquake: Energetic Slab Detachment. *Geophys. Res. Lett.*, 44(23), 11,824–11,832. doi:10.1002/2017GL076085